Nucl. Fusion 65 (2025) 106039 (15pp)

https://doi.org/10.1088/1741-4326/ae0801

Global gyrokinetic simulations of kinetic ballooning mode in NSTX-U plasmas

Tajinder Singh^{1,*}, Tariq Rafiq¹, Eugenio Schuster¹, Zhihong Lin² and Animesh Kuley³

E-mail: singh@lehigh.edu

Received 19 February 2025, revised 31 August 2025 Accepted for publication 17 September 2025 Published 25 September 2025



Abstract

Understanding the kinetic ballooning mode (KBM) is crucial for optimizing plasma performance in high- β spherical tokamaks. Global gyrokinetic simulations of KBMs in a projected NSTX-U shot are presented using realistic magnetic geometry and plasma profiles. Linear simulations across varying plasma β values show that the KBM is unstable in NSTX-U at significantly higher plasma β than conventional tokamaks due to the plasma shaping effects. Isotope effects on KBM are more pronounced at higher plasma β but remain relatively weak near the KBM stability threshold. Without flow shear, KBMs are unstable in both the core and pedestal regions. In the core, the investigated toroidal mode numbers in the range $n = [15, \dots, 31]$ are observed to be unstable. In the pedestal, on the other hand, the n = 15 mode is the most unstable mode due to local β values lower than those in the core. Parameter scans of plasma profile gradients and plasma β demonstrate that the linear KBM in the core exhibits a high sensitivity to β , whereas KBM in the pedestal shows a lower sensitivity. A reduction of β by approximately 15% from the projected value stabilizes KBMs in the core. Nonlinear simulations reveal that self-generated zonal flows play a crucial role in regulating KBM-driven turbulence, reducing the size of turbulent eddies, shortening the radial correlation length by nearly threefold, and decreasing turbulent transport by approximately 35%. These findings provide valuable insights into KBM stability and turbulent transport, offering guidance for optimizing operational scenarios in future experiments.

Keywords: spherical tokamaks, turbulent transport, gyrokinetic simulations

(Some figures may appear in colour only in the online journal)

Original Content from this work may be used under the terms of the Creative Commons Attribution 4.0 licence. Any further distribution of this work must maintain attribution to the author(s) and the title of the work, journal citation and DOI.

¹ Department of Mechanical Engineering and Mechanics, Lehigh University, Bethlehem, PA 18015, United States of America

² Department of Physics and Astronomy, University of California Irvine, Irvine, CA 92697, United States of America

³ Department of Physics, Indian Institute of Science, Bangalore 560012, India

^{*} Author to whom any correspondence should be addressed.

1. Introduction

The National Spherical Torus Experiment Upgrade (NSTX-U) [1] is designed to advance our understanding of fusion plasma physics by addressing critical knowledge gaps that impede the development of spherical tokamaks as practical fusion reactors. Building on the foundation established by the original NSTX [2], NSTX-U leverages its enhanced design to provide valuable insights into plasma behavior, making a significant contribution to the broader pursuit of practical fusion energy. Specifically, NSTX-U seeks to double the magnetic field, neutral beam injection (NBI) power, and plasma current while extending the pulse duration and improving plasma confinement. However, plasma confinement is limited by several processes, including turbulent transport, disruptions, and edgelocalized modes [3]. Among these, turbulent transport, caused by small-scale plasma instabilities, is a primary factor responsible for the transport of particles, energy, and momentum across the confining magnetic field [4, 5]. Therefore, understanding and mitigating turbulent transport in NSTX(U) is crucial for achieving sustained plasma confinement.

Numerous gyrokinetic simulation studies previously conducted on NSTX reveal the presence of various microinstabilities contributing to turbulent fluxes [6]. These instabilities are observed on scales both larger and smaller than the ion gyro-radius, which are henceforth referred to as 'ion scales' and 'electron scales', respectively. The ion scale instabilities include ion temperature gradient (ITG) modes, trapped electron modes (TEMs), kinetic ballooning modes (KBM), and micro-tearing modes (MTMs), while the electron scale instabilities include electron temperature gradient (ETG) modes. The ITG, TEM, and KBM instabilities can drive both ion and electron thermal transport, while instabilities such as MTM and ETG primarily contribute to electron thermal fluxes. High- β H-mode discharges in NSTX exhibit ion thermal transport at levels comparable to neoclassical predictions [7, 8], suggesting negligible ion turbulent heat transport. Local linear gyrokinetic simulations performed on various NSTX discharges with varying collisionality, as well as NSTX-U projections [9], indicate that ITG modes are stable, with thresholds approximately four times higher than experimental values for both NSTX and its projections. In contrast, KBMs are observed to lie near the threshold of the plasma profiles.

NSTX-U scenarios offer exciting opportunities for exploration, as data from various NSTX experiments indicate that global confinement scales inversely with collisionality [10, 11]. Notably, the collisionality in NSTX-U is expected to be more than six times lower than in NSTX, making the turbulent contribution to ion transport particularly intriguing under these conditions. While ITG modes are still expected to remain stable in NSTX-U, the role of KBM instabilities in driving ion turbulent transport remains uncertain due to their thresholds being close to the projected plasma profiles. As a result, KBM could significantly limit the achievable plasma profiles in NSTX-U. Additionally, most previous NSTX studies have relied on radially local simulations using flux-tube gyrokinetic

codes such as CGYRO [9]. However, for NSTX(U), $\rho^* \sim 1\%$, where ρ^* is the ratio of the ion gyro radius to the minor radius, indicating that global effects may play a significant role [12], in contrast to the asymptotic limit $\rho^* \to 0$, where the local simulations are expected to converge with global simulations [13]. Therefore, assessing the impact of finite ρ^* on turbulence characteristics is essential for determining the validity of local approximations in NSTX(U). In addition, recent local nonlinear gyrokinetic simulations of hybrid-KBM for the Spherical Tokamak for Energy Production (STEP), conducted without flow shear, require the radial width of the computational domain larger than the minor radius [14]. This finding underscores the importance of global simulations. Although a few studies in NSTX have used radially global codes, they are primarily limited to either the linear regime [15, 16] or the electrostatic regime [17]. This highlights the need for investigations into NSTX-U projections using global nonlinear electromagnetic gyrokinetic simulations, with a particular focus on KBM instability [18].

The Gyrokinetic Toroidal Code (GTC) [19] is a global particle-in-cell (PIC) code based on nonlinear gyrokinetic equations. This well-benchmarked code has been widely employed to investigate various aspects of fusion plasma physics, including turbulent transport [20], Alfvèn eigenmodes [21], radio frequency waves [22], and energetic particle transport [23]. GTC has been extensively used to study turbulent transport driven by micro-instabilities such as ITG and TEM in both tokamaks [24, 25] and stellarators [26, 27]. Moreover, GTC has been applied to simulate the KBM instability in conventional high aspect-ratio tokamaks, where the role of zonal flows was also examined [28]. Additionally, GTC has simulated the linear KBM instability in the pedestal region of H-mode discharges in the DIII-D tokamak. These simulations showed that the mode numbers and frequencies are consistent with experimental observations and the collisions have a negligible effect on KBM [29].

This work presents the first-ever global nonlinear electromagnetic gyrokinetic simulations for NSTX-U projections. The study focuses on the projection of NSTX discharge #121 123 to NSTX-U, generated using the TRANSP code, to investigate the KBM instability. GTC is used to perform both linear and nonlinear simulations for this high- β , high-temperature, low-collisionality discharge. Plasma equilibrium, density, and temperature profiles at the TRANSP simulation time t = 14.5 s are utilized for the analysis. To compare KBM characteristics between conventional high aspectratio tokamaks and the low aspect-ratio NSTX-U, linear simulations are performed for varying plasma β . Conventional tokamak-based plasma profiles with NSTX-U-like parameters are also used for benchmarking against earlier GTC simulations. These simulations reveal that the KBM threshold in NSTX-U is significantly higher than in conventional high aspect-ratio tokamaks, primarily due to low aspect-ratio and shaping effects. Simulations without compressional magnetic field fluctuations show no instability, indicating that the $\delta B_{||}$ term has a destabilizing influence on KBM, similar to other findings for NSTX [30]. In contrast to conventional tokamaks,

the amplitudes of the parallel and transverse magnetic field fluctuations are comparable.

The electrostatic simulations reveal that ITG is stable in NSTX-U, which is consistent with previous local simulations [9]. Linear simulations for hydrogen, deuterium, and tritium plasmas demonstrate that isotope effects become more pronounced at higher plasma β but are relatively weak near the KBM threshold. Plasma profile gradients are finite in the core and steep in the pedestal, providing a strong driving force for the instability. GTC simulations with realistic plasma profiles indicate KBM instability in both the core and pedestal regions. In the core, the investigated unstable toroidal mode numbers range from n = 15 to n = 31, whereas in the pedestal, the n = 15 mode is unstable due to lower plasma β values. The radial width of the mode structure is broad, highlighting the importance of global effects and nonlinear mode coupling near the mode-resonant flux surface. Parametric scans of plasma profile gradients and plasma β are conducted for the KBM in the core and pedestal. In the core, KBM is highly sensitive to plasma β , becoming stable after a ~15\% reduction in β_e , a value within projection uncertainties. Similarly, the ITG must be reduced by $\sim 30\%$ to stabilize KBM. In contrast, the KBM in the pedestal is less sensitive to plasma profile gradients and plasma β .

Nonlinear simulations assess the role of zonal flow in regulating KBM-driven turbulence which reveal that zonal flow acts as a regulatory mechanism, breaking large turbulent eddies into finer structures, reducing the amplitude of turbulent fluctuations by a factor of two and the transport by almost 35%. Additionally, 2D and 1D correlation functions for nonlinear electrostatic potential fluctuations show that zonal flow reduces the radial correlation length of turbulent eddies by threefold. Nonlinear simulations with hydrogen and deuterium plasmas indicate that turbulent fluctuations and transport are nearly identical for both isotopes. In this study, the $\vec{E} \times \vec{B}$ flow shear resulting from the equilibrium radial electric field, which has a magnitude comparable to the growth rate of the KBM at most radial locations, is not included. This suggests that the flow shear can have an additional stabilizing effect on the linearly unstable KBM and can reduce the associated nonlinear turbulent transport. These aspects will be addressed in future research.

The remainder of the paper is organized as follows. Section 2 presents the model equations used to simulate KBM. Section 3 discusses the simulations of KBM in the NSTX-U projection. Finally, the conclusions are summarized in section 4.

2. Gyrokinetic model equations for KBM simulations

This section provides a brief overview of the model equations implemented in GTC to simulate electromagnetic instabilities. Since the NSTX-U plasma under investigation corresponds to a low-collisionality discharge, collisions are neglected in this study. The gyro-averaged Vlasov equation, which describes

the toroidal plasma in an inhomogeneous magnetic field in 5D phase space [31–33], is expressed as:

$$\frac{\mathrm{d}}{\mathrm{d}t}f_{i}\left(\vec{X},\mu,\nu_{\parallel},t\right) = \left[\frac{\partial}{\partial t} + \dot{\vec{X}}\cdot\nabla + \dot{\nu}_{\parallel}\frac{\partial}{\partial\nu_{\parallel}}\right]f_{i}\left(\vec{X},\mu,\nu_{\parallel},t\right) = 0,$$
(1)

where f_i is the ion gyro-center distribution function and \vec{X} , ν_{\parallel} , μ represent the coordinates for the guiding center position of the particle, parallel velocity, and magnetic moment, respectively. The following equation describes the time evolution of the guiding center

$$\dot{\vec{X}} = v_{\parallel} \frac{\vec{B}_0^* + \delta \vec{B}_{\perp}}{B_0^*} + \vec{v}_E + \vec{v}_d + \vec{v}_{B_{\parallel}} + \vec{v}_{ZF}, \tag{2}$$

where $\vec{B}_0^* = \vec{B}_0 + \frac{B_0 v_\parallel m_i c}{Z_i B_0^*} \nabla \times \hat{b}_0$ is the modified magnetic field resulting from the transformation from particle space to the guiding center space, $B_0^* = B_0 + \frac{v_\parallel m_i c}{Z_i} \hat{b}_0 \cdot \nabla \times \hat{b}_0$ and $\delta \vec{B}_\perp$ is the perpendicular component of magnetic field fluctuations. The $\vec{E} \times \vec{B}$ drift is represented as $\vec{v}_E = \frac{c \hat{b}_0 \times \nabla \phi}{B_0^*}$, where the electrostatic potential ϕ is comprised of the fluctuating part $\delta \phi$ and the zonal component $\phi_{\rm ZF}$. The magnetic drift is represented as $\vec{v}_d = \vec{v}_c + \vec{v}_g$ which is comprised of curvature drift $\vec{v}_c = \frac{v_\parallel^2}{\Omega_i} \nabla \times \hat{b}_0$ and drift due to the gradient of magnetic field $\vec{v}_g = \frac{\mu}{m_i \Omega_i} \hat{b}_0 \times \nabla B_0$, where $\hat{b}_0 = \vec{B}_0/B_0$. The drift due to the parallel magnetic field fluctuations is $\vec{v}_{B_\parallel} = \frac{\mu c}{Z_i} \frac{\hat{b}_0 \times \nabla \delta B_\parallel}{B_0^*}$ and the drift due to zonal flow is $\vec{v}_{\rm ZF} = \frac{c \hat{b}_0 \times \nabla \phi_{\rm ZF}}{B_0^*}$, where $\delta B_\parallel = \hat{b}_0 \cdot \nabla \times \delta \vec{A}_\perp$ and c is the speed of light. The mass, charge, and cyclotron frequency of the ions are represented as m_i , Z_i , and Ω_i , respectively. The following equation describes the time evolution of the parallel velocity

$$\dot{v}_{\parallel} = -\frac{1}{m_{i}} \frac{\vec{B}_{0}^{*} + \delta \vec{B}_{\perp}}{B_{0}^{*}} \cdot \left(\mu \nabla B_{0} + Z_{i} \nabla \left(\phi + \mu \delta B_{\parallel} \right) \right)
- \frac{Z_{i}}{m_{i} c} \frac{\partial A_{\parallel}}{\partial t},$$
(3)

The electrostatic potential is calculated from the gyrokinetic Poisson equation, while the parallel and perpendicular components of the vector potential are calculated from the gyrokinetic parallel and perpendicular Ampere's equations, respectively. GTC uses the δf method [34] to reduce the marker particle noise. In this method, the particle distribution function is written as the sum of the equilibrium part and the fluctuating part, $f_i = f_{0i} + \delta f_i$. Therefore, equation (1) can be written as $Lf_i = 0$, where the differential operator is $L = L_0 + L_{ZF} + \delta L$,

$$L_0 = \frac{\partial}{\partial t} + \left(v_{\parallel}\hat{b}_0 + \vec{v}_d\right) \cdot \nabla - \frac{\mu}{m_i}\vec{B}_0^* \cdot \frac{\nabla B_0}{B_0} \frac{\partial}{\partial v_{\parallel}}, \tag{4}$$

$$L_{\rm ZF} = \vec{v}_{\rm ZF} \cdot \nabla - \frac{Z_i}{m_i} \frac{\vec{B}^* + \delta B_{\perp}}{B_0} \cdot \nabla \phi_{\rm ZF} \frac{\partial}{\partial v_{\parallel}}, \quad (5)$$

and

$$\delta L = \left(v_{\parallel} \frac{\nabla \times A_{\parallel} \hat{b}_{0}}{B_{0}^{*}} + \vec{v}_{E} + \vec{v}_{B_{\parallel}}\right) \cdot \nabla - \frac{1}{m_{i}} \left(\frac{\nabla \times A_{\parallel} \hat{b}_{0}}{B_{0}}\right)$$

$$\cdot \mu \nabla B_{0} - Z_{i} \frac{\vec{B}^{*} + \delta B_{\perp}}{B_{0}} \nabla \left(\delta \phi + \mu \delta B_{\parallel}\right) \frac{\partial}{\partial v_{\parallel}}$$

$$- \frac{Z_{i}}{m_{i}} \frac{\partial A_{\parallel}}{\partial t} \frac{\partial}{\partial v_{\parallel}}.$$
(6)

The equilibrium part f_{0i} satisfies $L_0f_{0i}=0$ and can be approximated as a local Maxwellian (i.e. ignoring neoclassical effects) as $f_{0i}=n_0\left(\frac{m_i}{2\pi\,T_i}\right)^{\frac{3}{2}}\exp\left(-\frac{m_iv_\parallel^2+2\mu B_0}{2T_i}\right)$. The perturbed part δf_i is calculated from the particle weight $\mathbf{w}_i=\delta f_i/f_i$ using the following equation

$$\frac{\mathrm{dw}_{i}}{\mathrm{d}t} = -\left(1 - \mathrm{w}_{i}\right) \left[\left(v_{\parallel} \frac{\nabla \times A_{\parallel} \hat{b}_{0}}{B_{0}} + \vec{v}_{\mathrm{ZF}}\right) \cdot \frac{\nabla f_{0i}}{f_{0i}} - \frac{1}{m_{i} f_{0i}} \frac{\partial f_{0i}}{\partial v_{\parallel}} \right. \\
\times \left(\frac{\nabla \times A_{\parallel} \hat{b}_{0}}{B_{0}} \cdot \mu \nabla B_{0} - \frac{\vec{B}^{*}}{B_{0}} Z_{i} \nabla \left(\delta \phi + \phi_{\mathrm{ZF}} + \mu \delta B_{\parallel}\right) \right) \\
\times - \frac{Z_{i}}{m_{i}} \frac{1}{f_{0i}} \frac{\partial f_{0i}}{\partial v_{\parallel}} \frac{\partial A_{\parallel}}{\partial t} \right]. \tag{7}$$

GTC employs a field-aligned mesh to represent the fluctuating quantities as it offers the maximum numerical accuracy and computational efficiency for the turbulence simulations. The parallel magnetic field fluctuations [32] and the equilibrium current density [35] are kept in the simulations as they provide an additional drive to KBM. The simulations presented here are fully electromagnetic which involve the calculations of electrostatic perturbed potential $\delta \phi$, parallel magnetic vector potential fluctuations $\delta A_{||}$, and parallel magnetic field fluctuations $\delta B_{||}$. The electrostatic potential is calculated from the gyrokinetic Poisson equation. The parallel magnetic vector potential is obtained from the parallel electric field [36]. The parallel magnetic field fluctuations are obtained from equation (14) of [32].

Since KBM dynamics are primarily governed by thermal ion kinetic effects, previous studies using GTC in high aspectratio conventional tokamaks have shown that kinetic electrons have a negligible impact on the KBM growth rate compared to fluid electrons [37]. Consequently, the current KBM simulations employ a massless electron fluid equation [28] within the lowest-order fluid-kinetic electron hybrid model [38]. In this approach, the electron distribution function is decomposed into an adiabatic part (computed using a massless electron fluid equation) and a non-adiabatic part (determined by the electron drift kinetic equation). The detailed procedure for solving this set of equations can be found in [32]. Additionally, the fluid description of electrons is sufficient for the present work, as recent local linear gyrokinetic simulations of the analyzed discharge indicate the presence of KBMs at most radii [9]. However, given the relatively large trapped electron population in NSTX-U, resulting from its low aspect-ratio and lowcollisionality, future studies should investigate the effects of trapped electrons on KBM dynamics.

3. KBM simulation results for NSTX-U plasmas

This section presents the global gyrokinetic simulations of the KBM instability in one of the projected discharges of NSTX-U. The NSTX-U discharge used for the GTC simulations is generated using the TRANSP code. The effects of plasma shaping and isotopes on KBM at higher plasma beta, compared to conventional tokamaks [37], are elucidated using cyclone-based profiles with parameters similar to the realistic profiles of NSTX-U. Following this, realistic profiles are employed to carry out the linear KBM simulations in the core and pedestal regions of NSTX-U. Sensitivity analysis explores the effect of plasma profile gradients and electron β on KBM growth rates and frequencies in the core and pedestal regions. Nonlinear simulations of KBM that emphasize the role of zonal flow in reducing turbulent fluctuations, transport and the radial correlation length are presented.

3.1. NSTX-U equilibrium and plasma profiles

The NSTX-U discharge used in these simulations is derived from NSTX discharge #121 123 and generated using the transport code TRANSP [39], corresponding to TRANSP ID 12 1123K55. These discharges represent low-collisionality, high-performance plasma scenarios for NSTX-U based on certain assumptions [40]. The TRANSP run used to generate the discharge is based on an NSTX discharge in which experimental profile shapes for electron density and temperature are used, with the density scaled to achieve a different Greenwald fraction. Ion thermal fluxes were assumed to be dominated by neoclassical transport, and the electron temperature was adjusted to match energy confinement time scalings. As a result, the projected temperatures are higher than those of the NSTX discharges due to increased field strength and heating power. The plasma equilibrium and kinetic profiles for the plasma species used in the simulations correspond to the TRANSP simulation time t = 14.5 s, with the Greenwald density limit set to 0.55. This projected discharge also features higher plasma temperatures and temperature gradients, making it a suitable candidate for studying the KBM. This discharge has previously been used for the linear local gyrokinetic analysis of ion-scale plasma instabilities [9], where KBMs are found to be unstable at most radii.

Figure 1 shows the equilibrium (a), safety factor and electron β profiles (b) for NSTX-U projected discharge #121 123. The major and minor radii are $R_0 = 1.04\,\mathrm{m}$ and $a = 0.54\,\mathrm{m}$, respectively. NSTX-U features a highly elongated plasma. KBM is highly sensitive to plasma equilibrium implementations [41]. Differences in geometric coordinates and the treatment of local versus global profiles can lead to significant variations in the real frequency and growth rate of the KBM instability. Additionally, the Shafranov shift may have a stabilizing effect on KBM. In contrast, the real frequency and growth rate of electrostatic instabilities, such as ITG and TEM, depend primarily on the location of the peak global profile gradients. GTC utilizes a realistic tokamak geometry generated by EFIT [42]. The numerical plasma equilibrium and profiles are transformed from toroidal coordinates (R, Z, φ)

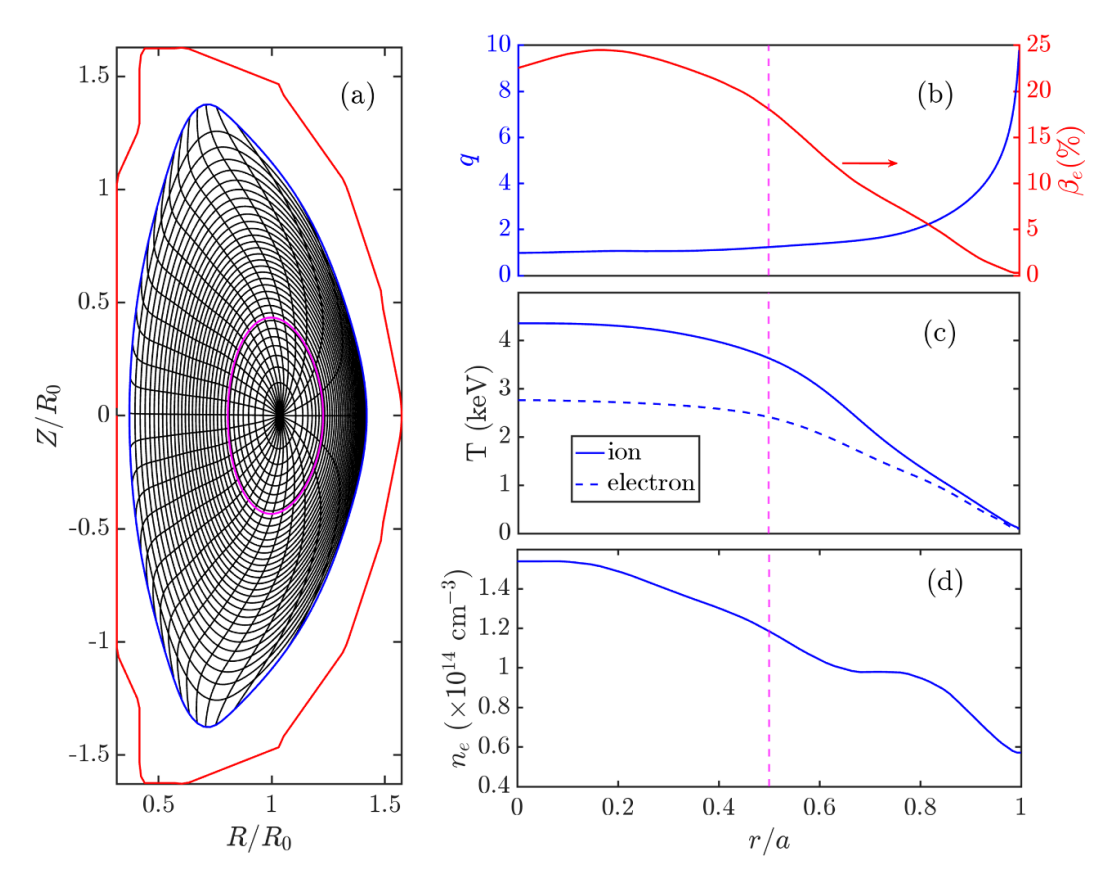


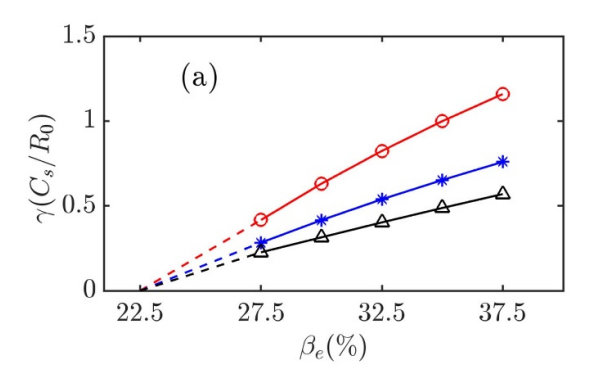
Figure 1. (a) Equilibrium of NSTX-U projected discharge #121 123 with TRANSP ID 12 1123K55. The black lines are drawn along constant ψ and θ in the magnetic coordinates, the magenta line shows the flux surface at r=0.5a, the blue line represents the last closed flux surface (LCFS), and the red line indicates the limiter. (b) The safety factor and electron β profiles as a function of the minor radius. The vertical magenta dashed line indicates the radial location r=0.5a. (c) The ion and electron temperature profiles as a function of minor radius. (d) The electron density profile as a function of minor radius.

to magnetic coordinates (ψ, θ, ζ) . The equilibrium magnetic field satisfies $\nabla \cdot \vec{B}_0 = 0$; however, the fluctuating magnetic field $\delta \vec{B}$ does not strictly satisfy $\nabla \cdot \delta \vec{B} = 0$ due to higher-order terms of order $\mathcal{O}(1/k_{\perp}L_B)$, which are neglected in the governing equations [43], where $1/L_B$ is the magnetic field gradient scale length. Furthermore, a finer turbulence mesh, with a size on the order of the gyro-radius, is generated by interpolating from the coarse equilibrium mesh using B-splines. This finer mesh is necessary for accurately simulating turbulent transport. Figure 1 also shows the temperature profiles for ions and electrons (c) and plasma density profile (d). The on-axis values of the ion and electron temperatures are 4.4 keV and 2.8 keV, respectively. The on-axis electron density is $1.5 \times 10^{14} \, \text{cm}^{-3}$. These parameters correspond to the on-axis $\beta_e = 22.5\%$, where the electron β is defined as $\beta_e = 8\pi n_e T_e/B^2$. Additionally, the electron density profile, in contrast to the temperature profiles, exhibits pronounced 'ears' that emerge shortly after the L-to-H transition, likely indicating the formation of an edge particle transport barrier caused by electron density buildup at the plasma boundary due to carbon fueling of the edge [44].

3.2. GTC simulations setup

Since the KBM instability is highly sensitive to boundary conditions, a large radial domain of NSTX-U is included in the

GTC simulations, covering $\psi \sim [0.02, 1.0] \psi_X$ in flux coordinates, where ψ_X is the magnetic flux at the last closed flux surface (LCFS). This translates to $r \sim [0.16, 1.0]a$ in radial coordinates, where r is the local minor radius. This approach ensures that the simulation results are unaffected by the application of the Dirichlet boundary condition, which sets the fluctuation quantities to zero at both ends of the simulation domain. The region near the magnetic axis is excluded from the simulations, as the plasma profiles are nearly flat in that region, with negligible instability drive due to the vanishingly small gradients. This choice will be further justified in the following discussion. The GTC parameters are optimized through convergence studies. For the turbulence mesh, the simulations use 100 grid points in the radial direction, 400 grid points in the poloidal direction, and 32 grid points in the parallel direction. The simulations utilize 50 marker particles per cell. The time step size is $\Delta t = 0.01R_0/C_s$, where C_s is the ion sound speed given by $C_s = \sqrt{T_e/m_i}$. For the NSTX-U equilibrium and plasma profiles, $C_s/R_0 = 3.5 \times 10^5 \text{ s}^{-1}$. In the convergence tests, the grid resolution is doubled and the number of marker particles per cell is increased by a factor of four. Under these changes, the simulation results, such as growth rates, remain within approximately 5% of the baseline case. The simulation grid size is nearly identical in the radial and poloidal directions and is given by $\Delta r \sim r\Delta\theta \sim 0.5\rho_i$, where



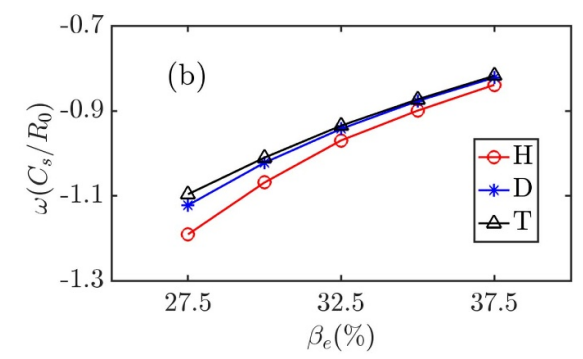


Figure 2. The variation of the growth rate (*a*) and frequency (*b*) for the n = 15 mode with the electron β represented in terms of on-axis values. The red lines with open circles represent hydrogen plasma, the blue lines with asterisks represent deuterium plasma, and the black lines with triangles represent the tritium plasma. The dashed lines represent the extrapolation to depict the threshold.

 $\rho_i = v_i m_i c / e B_0$ is the ion gyro-radius and $v_i = \sqrt{T_i / m_i}$. This work represents an initial step in simulating KBMs in spherical tokamaks using GTC, where a single toroidal mode is retained while multiple poloidal modes are included. Performing fully nonlinear multi-n simulations for KBMs in NSTX-U geometry presents significant numerical and computational challenges. These include the need for increased resolution, finer time stepping, and substantial computational resources to accurately capture nonlinear mode coupling and energy cascades. As such, the present study focuses on single-n simulations to isolate the characteristics of individual KBM and the regulation by zonal flow. Future studies could extend this approach by incorporating multiple toroidal modes to gain a more comprehensive understanding. Additionally, the simulations presented here assume a fixed plasma equilibrium while scanning profile parameters such as electron β and profile gradients. A typical linear or nonlinear GTC simulation of KBM is performed using 6 nodes on the Perlmutter supercomputer at NERSC with a walltime of approximately 3 hours. Each CPUonly compute node of Perlmutter is equipped with $2 \times AMD$ EPYC 7763 CPUs, with a base clock speed of 2.45 GHz. Each CPU has 64 cores, resulting in a total computational cost of approximately 2300 CPU hours per simulation.

3.3. Plasma shaping and isotope effects

Plasma shaping is known to improve the performance of NSTX [45]. In particular, shaped plasmas have a stabilizing effect on linear instabilities and nonlinear transport driven by micro-instabilities [46, 47]. To elucidate the effect of plasma shaping on KBM in NSTX-U, we have extended the previous work by GTC in high aspect-ratio conventional tokamaks with circular plasma using the cyclone-based plasma profiles, where the KBM was found to be unstable at $\beta_e \sim 1\%$ [37]. With the highly-elongated plasma in NSTX-U, the effect of plasma shaping on the KBM is investigated by exploring the dependence of growth rate and frequency of the KBM on the electron β while using the cyclone-based profiles, similar to those used in prior KBM studies for conventional high aspect-ratio tokamaks, with the typical plasma profile parameters of

NSTX-U as depicted in figure 1. This choice enables a comparison of KBM characteristics between NSTX-U and conventional high aspect-ratio tokamaks. The electron β is varied by scaling the on-axis electron density while keeping other profile parameters and gradients fixed. Figure 2 illustrates the variation of the growth rate (a) and frequency (b) of the KBM with toroidal mode number n = 15 for hydrogen, deuterium, and tritium plasmas as a function of electron β . The mode growth rate increases almost linearly with β_e for all the cases. The negative frequencies indicate that the mode propagates in the ion diamagnetic direction. The KBM frequencies are nearly identical for all the cases. The KBM growth rate is lower for the heavier isotope due to the slower response of the heavier ions, which have lower thermal speeds and respond more slowly to fluctuations [48]. Isotope effects become more pronounced at higher plasma β , but remain weak near the threshold. Mode diagnostics are conducted at the radial location $r \sim 0.5a$, corresponding to $\psi \sim 0.22\psi_X$ with $q \sim 1.2$. The linear instability threshold is determined by extrapolating the simulation data and is marked by the dashed lines. For all the three cases, the threshold occurs at $\beta_e \sim 22.5\%$, which matches the on-axis β_e for realistic plasma profiles in NSTX-U (see figure 1(b)). The nearly identical KBM instability thresholds observed across H, D, and T plasmas can be attributed to the threshold being governed primarily by macroscopic MHD parameters-namely the normalized pressure gradient and magnetic geometry-which are largely independent of ion mass. This is consistent with our simulations, which show that the threshold electron beta (β_e) remains approximately the same $(\sim 22.5\%)$ for all three isotopes. Moreover, our study demonstrates that the KBM threshold in NSTX-U is significantly higher than in conventional high aspect-ratio tokamaks (where $\beta_{\rm e} \sim 1\%$), a difference attributed to NSTX-U's low aspectratio and strongly shaped magnetic geometry. This highlights that magnetic shaping and global geometry have a dominant influence on the KBM threshold, further supporting the interpretation that the onset condition is largely mass-independent but sensitive to MHD equilibrium properties. In contrast, the KBM growth rates above the threshold vary with isotope mass due to kinetic effects, including differences in ion thermal speed, finite Larmor radius (FLR), and inertial response. These

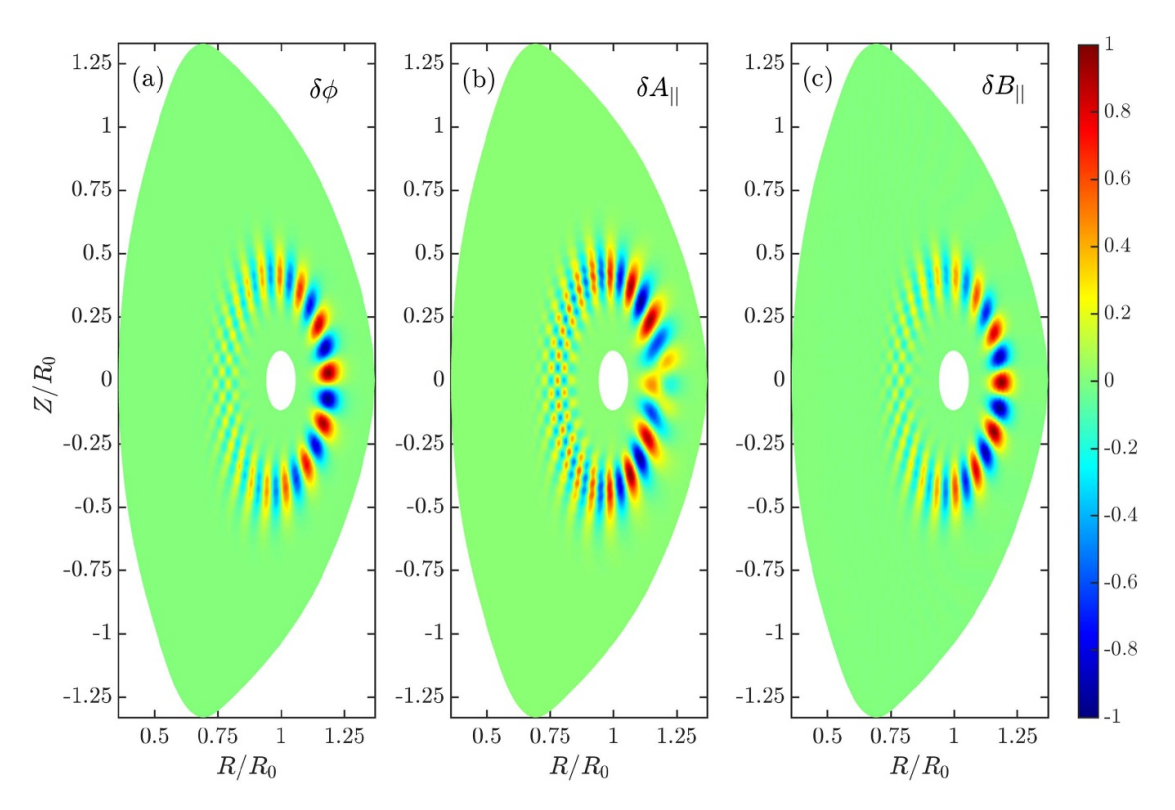


Figure 3. The 2D contour plots of the (a) electrostatic potential $\delta \phi$, (b) parallel magnetic vector potential $\delta A_{||}$, and (c) parallel magnetic field fluctuations $\delta B_{||}$ on the poloidal plane for n=15 mode. The amplitudes are normalized with the maximum values.

factors influence the instability's growth dynamics but not its onset. Therefore, the β_e scan shows that the KBM lies at the threshold for NSTX-U plasmas. Additionally, the KBM threshold in NSTX-U is much higher than in conventional high aspect-ratio tokamaks, where the threshold is $\beta_e \sim 1\%$ [37]. The stabilization of KBM at low plasma β is attributed to the highly elongated plasma shape of NSTX-U, unlike conventional tokamaks.

Figure 3 presents 2D contour plots of electrostatic potential $\delta \phi$, parallel magnetic vector potential $\delta A_{||}$, and parallel magnetic fluctuations $\delta B_{||}$. The eigenmode structure is predominantly observed on the low magnetic field side with unfavorable curvature. The mode is situated at $r \sim 0.5a$ and extends radially over the range $r \sim [0.4, 0.7]a$. Simulations that exclude the compressional magnetic field component $\delta B_{||}$ reveal that the $\delta B_{||}$ term is essential for the onset of KBM instability [30, 49]. The amplitudes of the parallel (δB_{\parallel}) and transverse (δB_{\perp}) magnetic field fluctuations are comparable, as discussed in detail in section 3.6. This behavior contrasts with that of KBMs in conventional tokamaks, where δB_{\parallel} is typically much smaller than δB_{\perp} [37]. Furthermore, simulations in the electrostatic limit, with both $\delta A_{||}$ and $\delta B_{||}$ terms turned off, show the absence of instability. This indicates that the electrostatic ITG instability is stable in NSTX-U, consistent with earlier findings from local gyrokinetic simulations [9].

Figure 4 displays the Fourier amplitudes of the poloidal harmonics of the electrostatic potential $\delta\phi$, parallel magnetic vector potential $\delta A_{||}$, and parallel magnetic fluctuations $\delta B_{||}$ as a function of the minor radius for the n=15 mode. The dominant poloidal harmonics for both $\delta\phi$ and $\delta B_{||}$ exhibit a Gaussian

profile. For $\delta A_{||}$, the dominant poloidal harmonics show odd parity around the mode rational surface (i.e. kink parity), and the amplitudes of the poloidal harmonics near this surface cancel each other out, thereby reducing the parallel magnetic vector potential fluctuations on the outer mid-plane side where the curvature is unfavorable. In contrast, the poloidal harmonics of $\delta \phi$ and $\delta B_{||}$ show even parity around the mode rational surface.

3.4. Linear KBM simulations in the core and pedestal

Linear simulations are performed for the KBM using the realistic plasma profiles of NSTX-U as shown in figure 1. Figure 5 shows the normalized ion and electron temperature gradients (a) and the normalized plasma density gradient (b) for the NSTX-U profiles. The normalized profile gradient is $R_0/L_f = -R_0 d(\ln f)/dr$, where $1/L_f$ is the inverse gradient scale length. The profile gradients are finite in the core and steep in the pedestal, illustrating that the KBM could be unstable in the core and pedestal regions.

Figure 6 illustrates the variation in the growth rate (a) and frequency (b) of the KBM as a function of the toroidal mode number. In the simulations, a single toroidal mode is evolved while the multiple poloidal modes are retained. The mode diagnostic is conducted at the radial location $r \sim 0.55a$. The unstable modes investigated here cover the range n = [15, 31]. The toroidal mode numbers n = 15 and n = 20 exhibit nearly identical growth rates, while the growth rate decreases as the toroidal mode number increases. Modes with higher toroidal mode numbers are stabilized due to FLR effects [50]. In addition, the kink drive term due to the equilibrium current has a

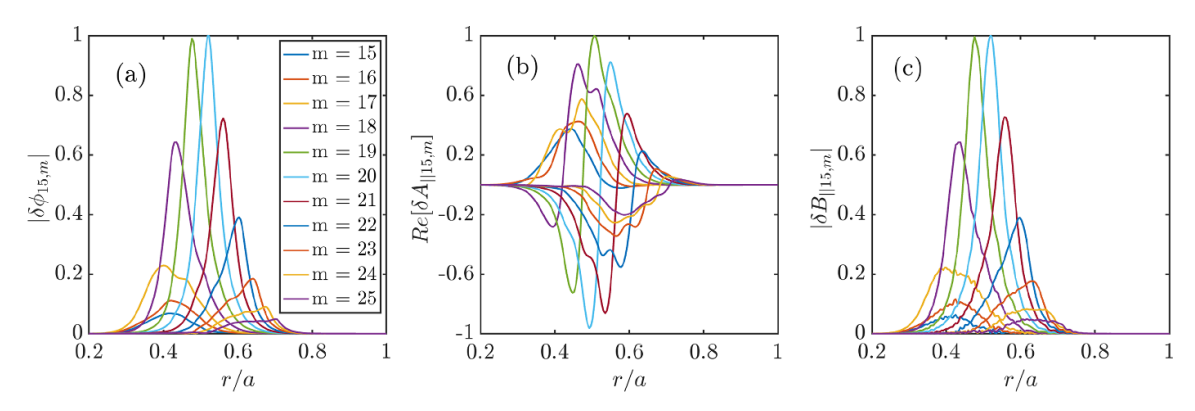


Figure 4. The radial profile of the different poloidal modes m of the electrostatic potential $\delta\phi$ (a), parallel magnetic vector potential $\delta A_{||}$ (b), and parallel magnetic field fluctuations $\delta B_{||}$ (c) for n=15 toroidal mode. The amplitudes are normalized by the maximum values.

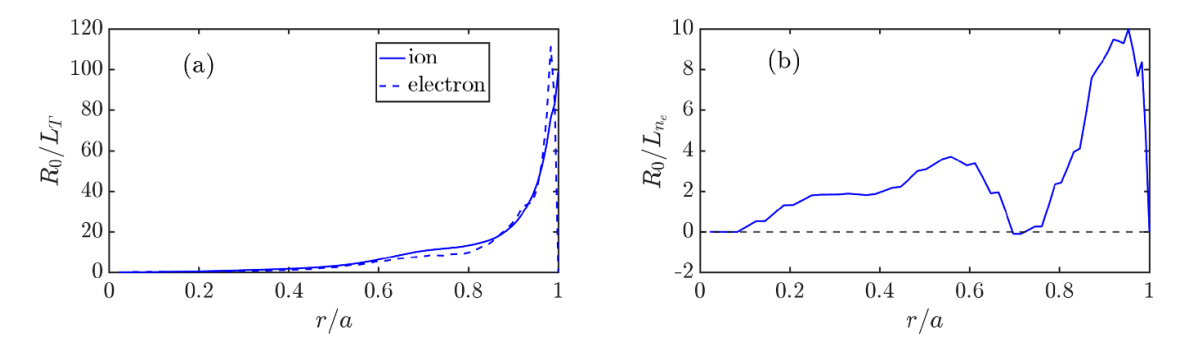


Figure 5. (a) The normalized temperature gradient for ion (solid) and electron (dashed), and (b) the normalized electron density gradient as a function of the minor radius for NSTX-U discharge #121 123. The dashed horizontal line represents the zero electron density gradient.

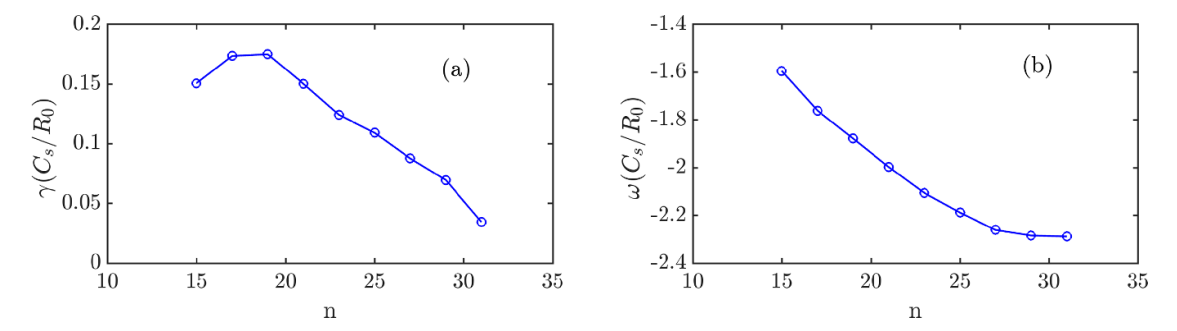


Figure 6. The variation of the (a) growth rate and (b) frequency of KBM in the core as a function of toroidal mode number n in the linear simulations.

negligible impact on the linear growth rate of KBMs (\sim 3%). The equilibrium current indirectly influences other magnetic quantities, such as the safety factor and magnetic shear, which are fully accounted for through the input equilibrium profiles.

KBM is found to be unstable in the pedestal region due to the presence of steep profile gradients. However, due to the relatively lower values of β_e in the pedestal compared to the core, only the n=15 mode becomes unstable out of the range of unstable toroidal modes investigated in the core. Figure 7 displays 2D contour plots of the electrostatic potential $\delta\phi$, parallel magnetic vector potential $\delta A_{||}$, and parallel magnetic fluctuations $\delta B_{||}$ illustrating the mode structure in

the core and pedestal regions. The parallel and perpendicular magnetic field fluctuations are of similar magnitude. In the core, the mode peaks at the radial location $r \sim 0.54a$ and spans the range $r \sim [0.41, 0.66]a$. In the pedestal, the mode is concentrated at the radial location $r \sim 0.83a$ and spans the range $r \sim [0.75, 0.92]a$. The mode diagnostics at $r \sim 0.83a$ show that the dominant mode in the pedestal, n = 15, m = 35, has a growth rate of $0.16C_s/R_0$ and a frequency of $0.40C_s/R_0$. The width of the KBM mode structure observed in our simulations is closely related to the spatial extent of the driving profile gradients. In both the core and pedestal regions, the gradients are relatively broad in radius, leading to extended drive

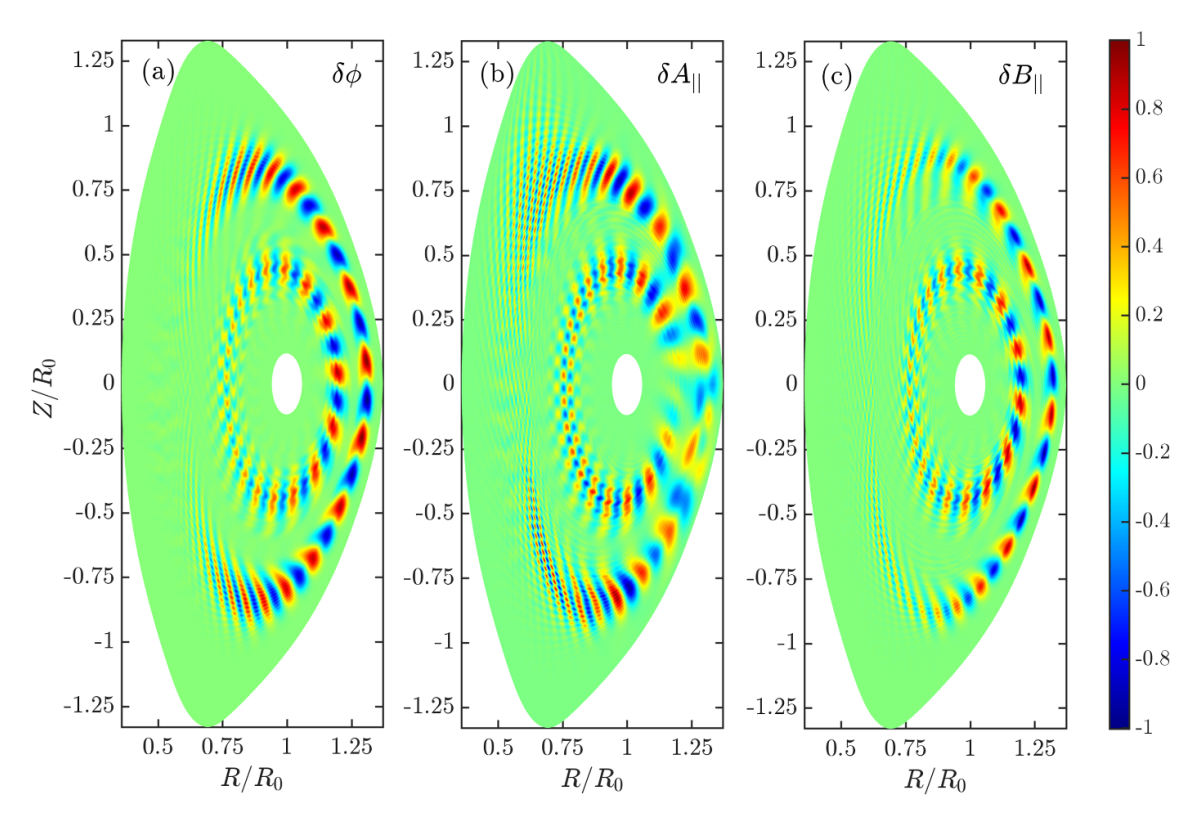


Figure 7. The 2D contour plots of the (a) electrostatic potential $\delta\phi$, (b) parallel vector potential δA_{\parallel} , and (c) parallel magnetic field fluctuations δB_{\parallel} on the poloidal plane for n=15 mode showing the instability in the core and pedestal regions. The amplitudes are normalized with the maximum values.

regions for the KBMs. As a result, the unstable eigenmodes develop a wider radial structure, which is often called radial streamer, than is typically seen in cases with more sharply localized gradients. It is important to note that the plasma profile includes a small region with a negative density gradient at $r \sim 0.7a$ (see figure 5(b)). As a result, the KBMs in the core and pedestal do not mix and remain distinct in the radial direction.

3.5. Sensitivity scans for plasma profile gradients and electron β

Figure 8 shows the variation in the growth rate and frequency of the n = 15 mode in the core and pedestal regions with the normalized profile gradients for plasma density, electron and ion temperature, and electron β . These scans are conducted by varying one parameter at a time while keeping the others fixed. The parameter X represents the factor by which the profile gradients and electron β are scaled relative to the actual values. The KBM becomes marginally stable in the core after reducing β_e by approximately 15% from the projected value, which is close to the experimental uncertainties. The ion temperature gradient scan indicates that the KBM becomes nearly stable after reducing it by about 30% from the projected value. In contrast, the KBM shows little sensitivity to the density and electron temperature gradients. Similarly, in the pedestal, the parameter scans suggest that the KBM is less affected by the profile gradient and electron β in the pedestal.

3.6. Nonlinear simulations and role of zonal flow

After an extensive linear simulation study of KBM, nonlinear simulations are performed by turning on the nonlinear terms in the gyrokinetic equations. Here, we restrict ourselves to the instability in the core region only, while suppressing the KBM in the pedestal. This choice ensures that the nonlinear simulation results remain unaffected by boundary effects, as the KBM in the core is situated sufficiently far from the simulation boundaries. Figure 9 presents the 2D contour plot of the electrostatic potential in the nonlinear simulation phase, both without (a) and with (b) zonal flow. Zonal flow (n = 0, m = 0)refers to poloidally and toroidally symmetric structures that vary in the radial direction. It is generated self-consistently through nonlinear interactions with the turbulence. In a KBMdominant plasma, zonal flows are nonlinearly generated by both Reynolds stress and Maxwell stress, which do not cancel each other due to deviation from the ideal Alfvén state. Also, the electromagnetic component can influence both the amplitude and structure of zonal flows, thereby affecting their ability to regulate KBM-driven turbulence. Zonal flow has a regulatory effect on turbulence, disrupting turbulent vortices by breaking them into smaller eddies. As a result, the amplitude of the turbulent fluctuations is reduced by nearly half due to the zonal flow's regulation. These results are consistent with earlier GTC simulations in conventional high aspect-ratio tokamaks [51] and stellarators [27], where turbulence regulation by zonal flows has been shown to play a significant role.

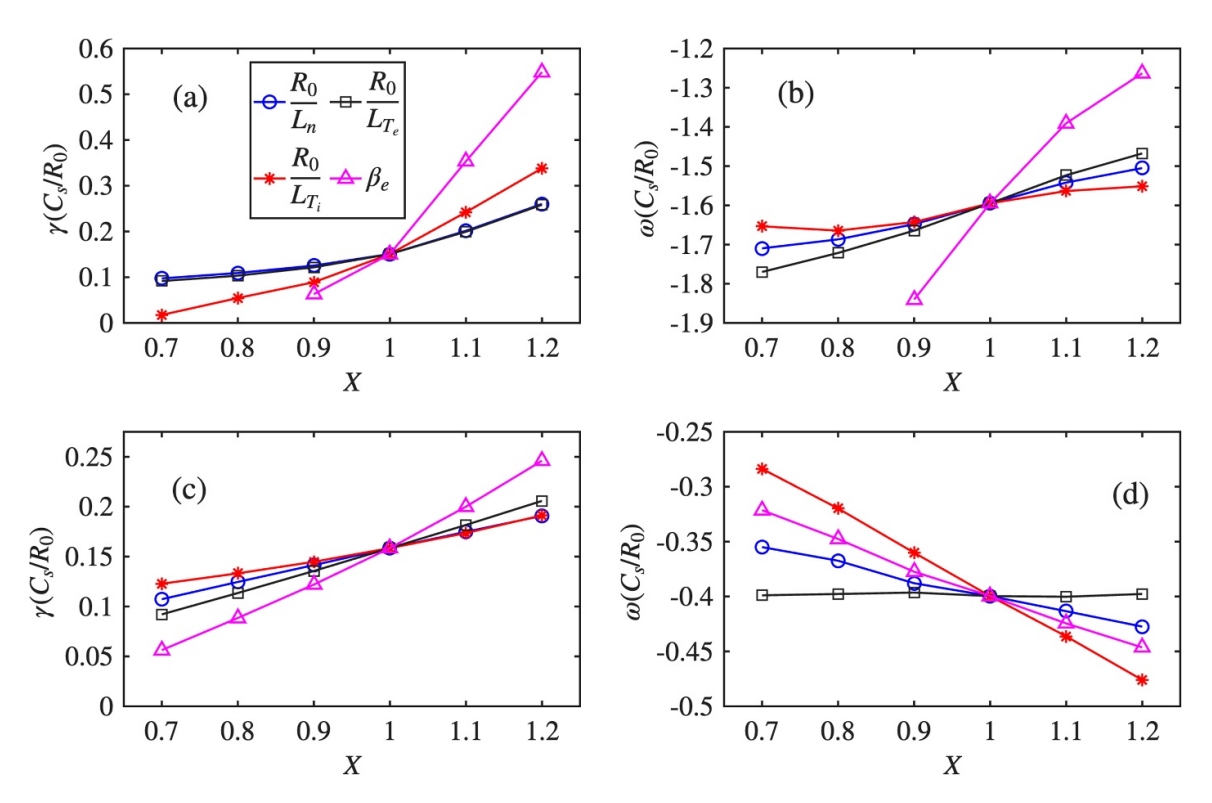


Figure 8. The variation of the growth rate (a), (c) and frequency (b), (d) of n = 15 mode in the core (a), (b) and pedestal (c), (d) regions with the normalized profile gradients for plasma density (o), electron (\Box) and ion (*) temperature, and the electron β (\triangle) .

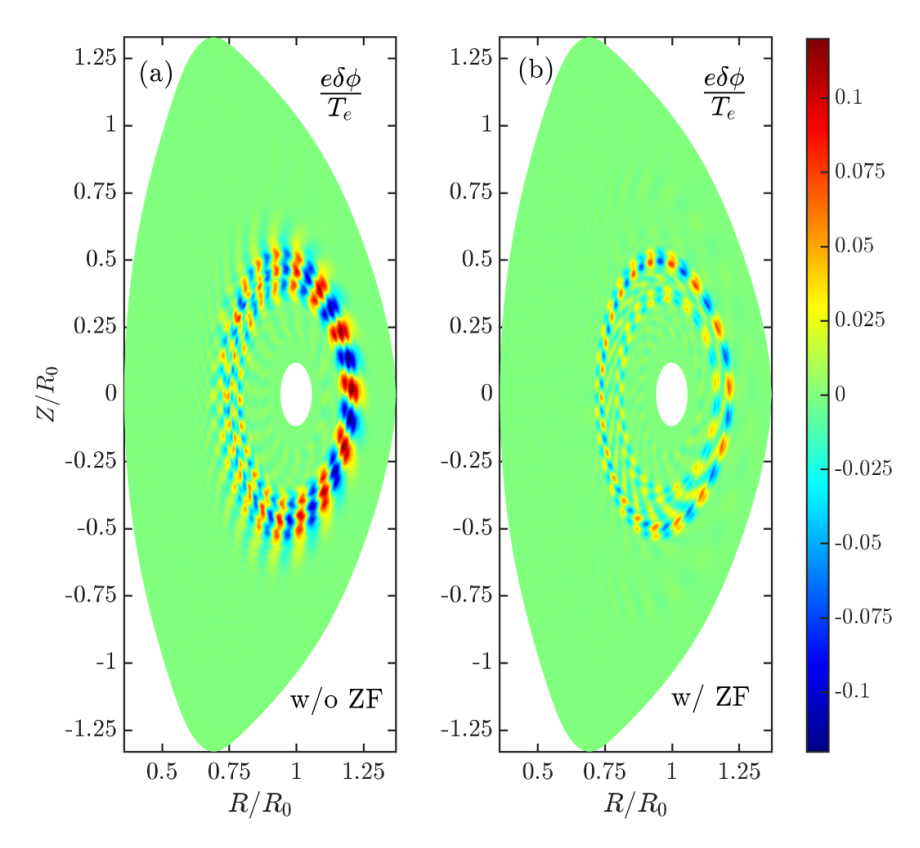


Figure 9. The 2D contour plots of the electrostatic potential $\delta \phi$ on the poloidal plane for n=15 mode, (a) without and (b) with zonal flow. The results correspond to the same physical time in the simulations.

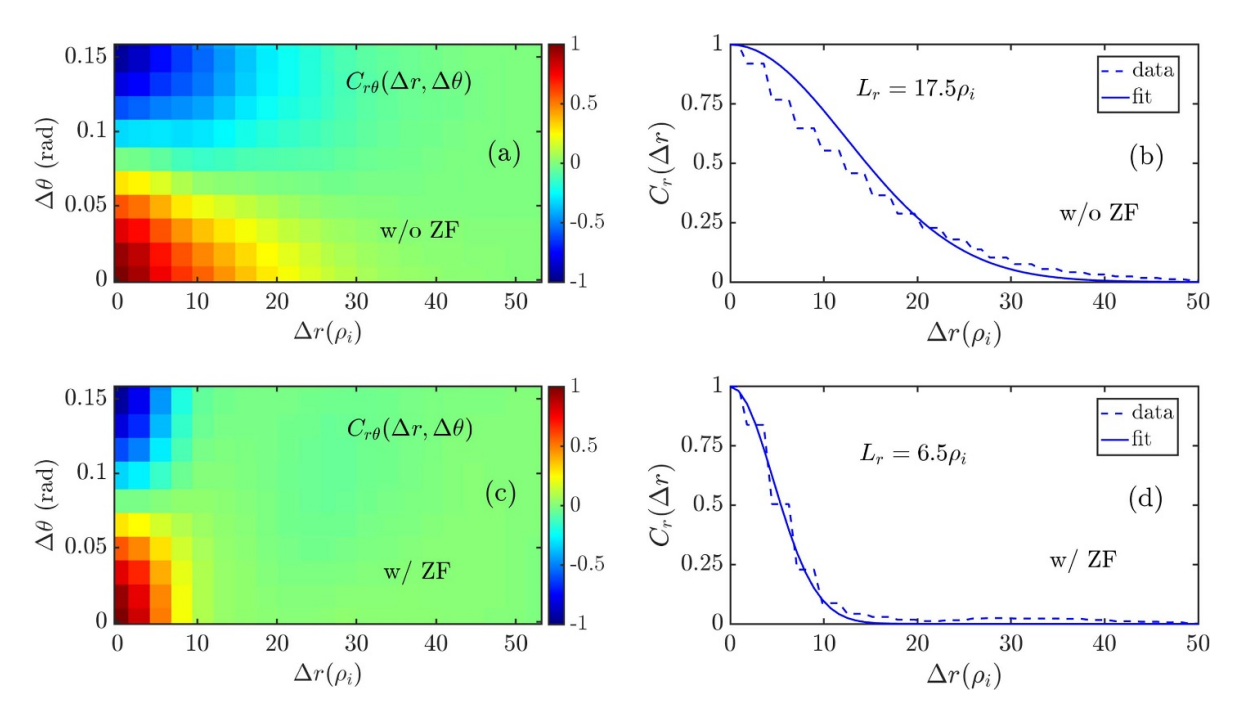


Figure 10. The 2D (a), (c) and 1D (b), (d) correlation functions without (a), (b) and with (c), (d) zonal flow, calculated from the eigenmode structures of $\delta \phi$ in the nonlinear phase of the simulations.

Additionally, the radial extent of the fluctuations suggests that nonlocal effects, such as turbulence spreading could play a significant role [52–54].

Figure 10 displays the 2D and 1D correlation functions, both without and with zonal flow, calculated from the eigenmode structures of the electrostatic potential $\delta\phi$ on the poloidal plane in the nonlinear phase of the simulations, as shown in figure 9. The presence of zonal flow reduces the radial correlation length of the turbulent eddies by nearly three times.

The radial correlation length of the turbulence is calculated from the following two-point correlation function:

$$C_{r\theta}\left(\Delta r, \Delta \theta\right) = \frac{\langle \delta \phi \left(r + \Delta r, \theta + \Delta \theta\right) \delta \phi \left(r, \theta\right) \rangle}{\sqrt{\langle \delta \phi^{2} \left(r + \Delta r, \theta + \Delta \theta\right) \delta \phi^{2} \left(r, \theta\right) \rangle}}, \quad (8)$$

where Δr and $\Delta \theta$ denote the radial and poloidal separations between the points, and $\langle \cdots \rangle$ represents the flux surface average. The 1D radial correlation function $C_r(\Delta r)$ is obtained by taking the maximal values along the ridge of the 2D correlation function, which exhibits a Gaussian decay: $C_r(\Delta r) \sim \exp(-(\Delta r/L_r)^2)$, where L_r is the radial correlation length.

The particle diffusivity and heat conductivity are calculated as follows

$$D = \frac{1}{\langle |\nabla \psi|^2 \rangle \frac{\partial n}{\partial \psi}} \left\langle \int d^3 \nu \delta f \vec{v}_{\rm E} \cdot \nabla \psi \right\rangle, \tag{9}$$

$$\chi_i = \frac{1}{\langle |\nabla \psi|^2 \rangle n_i \frac{\partial T_i}{\partial x^i}} \left\langle \int d^3 \nu \delta f_i \left(\frac{1}{2} m_i v^2 - \frac{3}{2} T_i \right) \vec{v}_E \cdot \nabla \psi \right\rangle, (10)$$

where $|\cdots|$ represents the absolute value.

Figure 11 presents the time history of ion heat conductivity and particle diffusivities for cases with and without zonal flow. The heat conductivity and particle diffusivity are expressed in

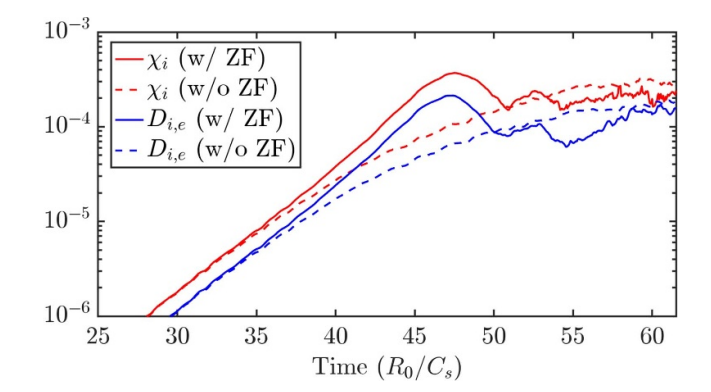
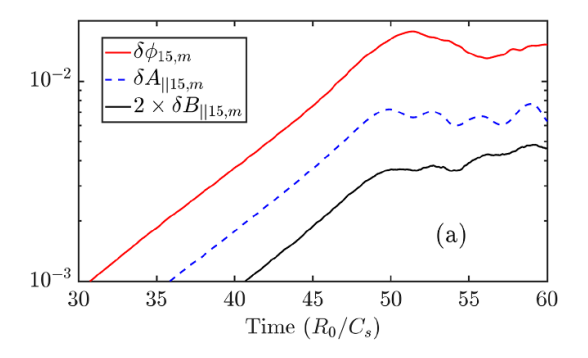


Figure 11. (a) The time history of the volume averaged ion heat conductivity (red lines) and ion and electron diffusivities (blue lines) for the simulations with (solid lines) and without (dashed lines) zonal flow.

Bohm units, $\chi_{\rm B} = D_{\rm B} = cT_{\rm e}/eB$. The turbulent fluctuations and associated transport initially increase during the linear phase of the simulations and then saturate. The presence of zonal flow reduces the saturated transport by approximately 35%. In addition, the ratio $D_i/\chi_i \sim 0.6$ for the simulations presented.

Figure 12(a) presents the time history of the electrostatic potential $\delta \phi$, parallel magnetic vector potential $\delta A_{||}$, and parallel magnetic field fluctuations $\delta B_{||}$ for the n=15 mode at the mode rational surface in the nonlinear simulations. The fluctuation amplitude increases exponentially during the linear phase of the simulations and then saturates in the nonlinear phase due to the coupling between various modes and the self-generated zonal flow. Figure 12(b) shows the time history of the zonal fields with the normalization similar to that of the perturbed fields. The zonal current is found to be significantly



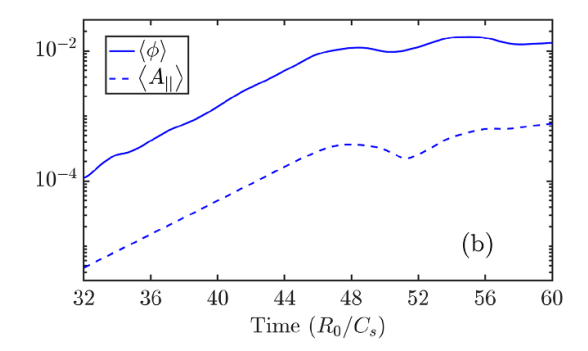
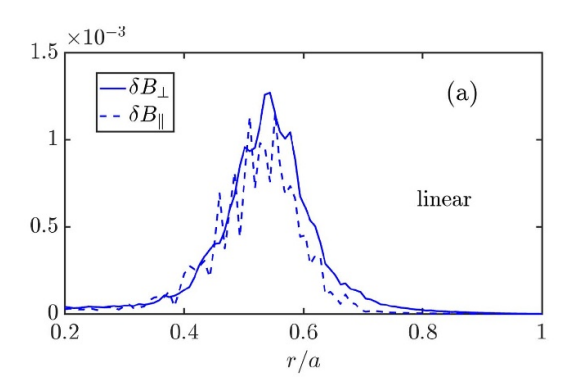


Figure 12. (a) The time history of the electrostatic potential, parallel vector potential, and parallel magnetic field fluctuations in the nonlinear simulations of n = 15 mode. The electrostatic potential is normalized with T_e/e , the parallel vector potential is normalized with T_e/ev_A , and the parallel magnetic field fluctuations are normalized by B_0 , where v_A is the Alfvén velocity. (b) The time history of the radially averaged zonal fields.



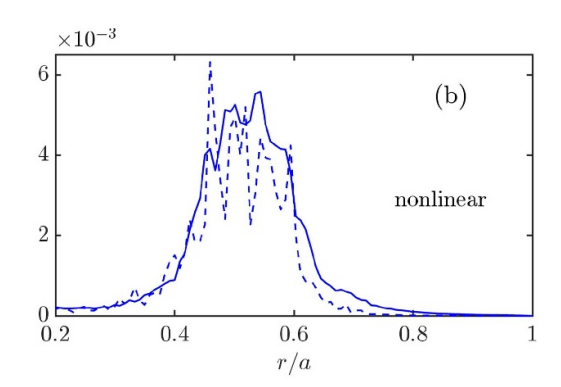
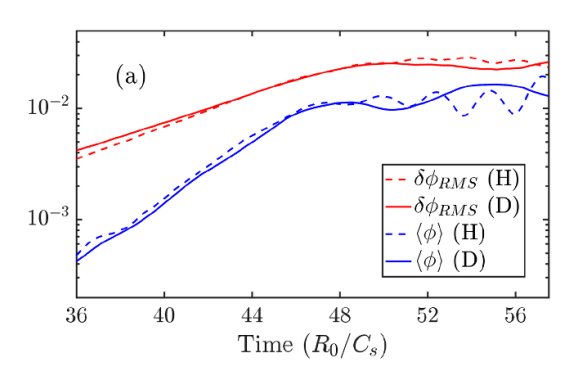


Figure 13. The radial variation of the root-mean-squared parallel and perpendicular magnetic field fluctuations (normalized by B_0) in the linear (a) and nonlinear (b) phase of the simulation.

smaller in magnitude compared to the zonal flow. Specifically, the zonal δB is much weaker (therefore, not shown here). As a result, their contribution to the nonlinear saturation dynamics is negligible in this case. Figure 13 shows the radial variation of the root-mean-squared magnetic field fluctuations in the parallel and perpendicular directions in the linear and nonlinear phase of the simulation. The amplitude of δB_{\parallel} fluctuations is comparable to that of δB_{\perp} fluctuations. This behavior contrasts with that observed in conventional high aspectratio tokamaks, where δB_{\parallel} is typically much smaller than δB_{\perp} , and its effects can often be neglected in KBM dynamics [29, 32]. In spherical tokamaks, however, the combination of low aspect-ratio and strong plasma shaping leads to δB_{\parallel} and δB_{\perp} fluctuations of comparable strength. These fluctuations are essential for the destabilization of the KBM, which is consistent with earlier linear local simulations [9] and highlights the critical role of the δB_{\parallel} term in the KBM physics of spherical tokamaks. It is important to note that in the GTC formulation, the perpendicular magnetic field fluctuations $\delta \vec{B}_{\perp}$ strictly satisfy $\nabla \cdot \delta \vec{B}_{\perp} = 0$, while $\nabla \cdot \delta \vec{B}_{\parallel}$ is not exactly zero due to neglected higher-order terms of order $\mathcal{O}\left(\frac{1}{k_{\perp}L_{B}}\right)$. For the present case, this approximation is well justified since $\frac{1}{k_{\perp}L_{R}}$ ~ 0.01. Moreover, the ratios $\frac{k_{\parallel}}{k_{\perp}} \sim 0.0046$ and $\frac{k_{\parallel} \delta B_{\parallel}}{k_{\perp} \delta B_{\perp}} \sim 0.0036$ are both very small. These values confirm that δB_{\parallel} contributes only weakly to $\nabla \cdot \delta \vec{B}$. While δB_{\parallel} and δB_{\perp} fluctuations are of comparable order in the NSTX-U case studied, their respective contributions to the divergence are strongly separated by the scale factor $k_{\parallel}/k_{\perp} \ll 1$.

Figure 14 shows the time history of the root-mean-squared electrostatic potential $\delta\phi_{\rm RMS}$ at r=0.55a and the radially averaged zonal potential $\langle\phi_{\rm ZF}\rangle$ (a), along with the time history of ion heat conductivities and ion and electron diffusivities (b) for both hydrogen and deuterium plasmas. A comparison of the results for hydrogen and deuterium plasmas reveals that the nonlinear phase shows nearly identical saturation levels of turbulent fluctuations, zonal flow, and transport for both ion species. The results for tritium plasma (not shown here) are identical to those of deuterium plasma. This suggests that at the projected plasma profiles that are close to the KBM threshold, isotope effects are negligible. Additionally, the oscillations observed in the nonlinear phase of the simulations correspond to the periodic recovery of the linear eigenmode structure due to the self-consistent interaction between turbulence and zonal flow.

In this work, the $\vec{E} \times \vec{B}$ flow shear due to the equilibrium radial electric field is not considered, which can have a significant impact on the linear growth rate of the instability and the turbulent transport associated with the KBM [55]. The flow shear can break turbulent eddies into finer eddies, thereby reducing the radial correlation length. Recent



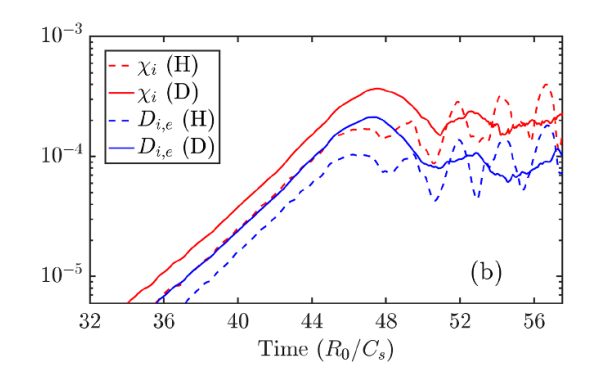


Figure 14. (a) The time history of the root-mean-squared electrostatic potential $\delta \phi_{RMS}$ at r=0.55a and the radially averaged zonal potential $\langle \phi \rangle$, (b) the time history of the volume averaged ion heat conductivity and ion and electron diffusivities for hydrogen (dashed lines) and deuterium (solid lines) plasmas.

GTC simulations of KBM instability in a conventional high aspect-ratio tokamak demonstrate that flow shear due to the radial electric field reduces the linear growth rate of the KBM by tilting the mode structure, which consequently reduces the turbulent transport [37]. Additionally, even larger flow shear has a stabilizing effect on the KBM and associated turbulence, which could be relevant in NSTX-U due to the injected torque from NBI heating and its relatively small moment of inertia. However, without delving into the detailed simulations which include the $\vec{E} \times \vec{B}$ shear, its effect on the KBM presented in this study can be accessed qualitatively. The shearing rate due to the flow shear at most of the radii for the analyzed NSTX-U discharge is comparable to the maximum growth rate of the KBM instability. Under such conditions, the flow shear could stabilize any linearly unstable KBM and suppress the associated nonlinear turbulence and transport. Additionally, the NSTX-U discharge used in this study presents a significant fraction of carbon impurity ions, in addition to thermal ions and electrons, which are not included in the simulations presented here. Previous GTC simulations in tokamaks [56] and stellarators [25] show a significant reduction in the linear growth rate of instability and turbulent transport due to the presence of impurity ions alongside thermal ions and electrons. Future work could investigate these stabilizing mechanisms of KBM in NSTX-U in detail. Furthermore, it is important to note that the NSTX-U discharge used in this work is a projection of its predecessor, NSTX, where some assumptions were made. It would be interesting to explore these possibilities further in the context of the realistic NSTX-U experiment.

4. Conclusions and discussion

This study presents the first global gyrokinetic simulations of KBM instability for future NSTX-U scenarios. Linear and nonlinear simulations are performed using the GTC, based on the NSTX-U projected discharge #121 123 generated by the TRANSP code, representing a high-temperature plasma with low-collisionality. Linear simulations show that the KBM threshold in NSTX-U is higher than in traditional high aspect-ratio tokamaks, primarily due to low aspect-ratio

and shaping effects. Simulations with hydrogen, deuterium and tritium as thermal ions reveal that KBM growth rates are higher in hydrogen plasma due to isotope effects. These effects are more pronounced at higher plasma β and diminish near the KBM threshold. For the analyzed discharge, KBM is unstable in both the core and pedestal regions when the flow shear due to the equilibrium radial electric field is neglected. In the core, toroidal mode numbers in the range n = [15, ..., 31] are observed to be unstable. In the pedestal, however, the n = 15 mode is the dominant unstable mode due to local β values lower than those in the core. The radial width of the KBM determines the significance of global effects on nonlinear mode coupling. Excluding parallel magnetic field fluctuations δB_{\parallel} in the simulations shows that this term is critical for KBM destabilization. Simulations without the δA_{\parallel} term confirm that the ITG mode remains stable in NSTX-U, consistent with prior studies. Additionally, in contrast to the conventional tokamaks, the parallel and transverse magnetic field fluctuations have comparable amplitudes. Sensitivity analyses of plasma profile gradients and plasma β reveal distinct behaviors in the core and pedestal regions. In the core, KBM is highly sensitive to plasma β , stabilizing when β is reduced by approximately 15%, a change within the experimental uncertainty. Similarly, reducing the ion temperature gradient by about 30% also stabilizes the KBM. In contrast, KBM in the pedestal region shows less sensitivity to plasma β and profile gradients. Nonlinear simulations highlight the role of self-generated zonal flows in regulating KBM-driven turbulence and transport. These flows disrupt turbulent eddies, breaking them into smaller structures, thus reducing their amplitude by nearly 50% and the turbulent transport by approximately 35%. Correlation analyses of electrostatic potential fluctuations in the nonlinear phase-both 2D and 1D-demonstrate that zonal flows shorten the radial correlation length of turbulent eddies by a factor of three. The $\vec{E} \times \vec{B}$ shearing rate is comparable to the maximum KBM growth rate at most radial locations. This suggests that flow shear could play an important role in stabilizing linearly unstable KBMs and suppressing turbulence and transport in NSTX-U. Future research could further investigate these stabilizing mechanisms.

Acknowledgments

This work is supported by the U.S. Department of Energy, Office of Science, under Award Numbers DE-SC0021385 and DE-SC0013977. The authors thank Y C Chen, G Y Sun, X Wei, H Huang, and the GTC Team for the helpful discussions. The authors extend their gratitude to J Parisi, T Adkins, J McClenaghan, and J Berkery for providing useful comments. This research has used resources of the National Energy Research Scientific Computing Center, a DOE Office of Science User Facility supported by the Office of Science of the U.S. Department of Energy under Contract No. DE-AC02-05CH11231 using NERSC award FES-ERCAP0031122. Z L acknowledges NERSC for providing a portion of the computational resources and is supported by the Office of Science of the U.S. Department of Energy grants with award numbers DE-SC0021316. A K thanks the Board of Research in Nuclear Sciences (BRNS sanctioned No. 57/14/04/2022-BRNS), the Science and Engineering Research Board EMEQ program (SERB sanctioned No. EEQ/2022/000144) and the National Supercomputing Mission (Ref No: DST/NSM/R&D_HPC_Applications/2021/4) for the computing time.

ORCID iDs

Tajinder Singh © 0000-0003-0860-3626 Tariq Rafiq © 0000-0002-2164-1582 Eugenio Schuster © 0000-0001-7703-6771 Zhihong Lin © 0000-0003-2007-8983 Animesh Kuley © 0000-0003-2325-6597

References

- [1] Berkery J.W. *et al* 2024 NSTX-U research advancing the physics of spherical tokamaks *Nucl. Fusion* **64** 112004
- [2] Ono M. et al 2000 Exploration of spherical torus physics in the NSTX device Nucl. Fusion 40 557
- [3] Doyle E.J. et al 2007 Progress in the ITER Physics Basis Chapter 2: Plasma confinement and transport Nucl. Fusion 47 S18
- [4] Horton W. 1999 Drift waves and transport Rev. Mod. Phys. 71 735–78
- [5] Kaye S.M., Connor J.W. and Roach C.M. 2021 Thermal confinement and transport in spherical tokamaks: a review *Plasma Phys. Control. Fusion* 63 123001
- [6] Guttenfelder W. et al 2013 Progress in simulating turbulent electron thermal transport in NSTX Nucl. Fusion 53 093022
- [7] Kaye S.M. et al 2007 Scaling of electron and ion transport in the high-power spherical torus NSTX Phys. Rev. Lett. 98 175002
- [8] Kaye S. et al 2007 Confinement and local transport in the National Spherical Torus Experiment (NSTX) Nucl. Fusion 47 499
- [9] Clauser C.F., Guttenfelder W., Rafiq T. and Schuster E. 2022 Linear ion-scale microstability analysis of high and low-collisionality NSTX discharges and NSTX-U projections *Phys. Plasmas* 29 102303
- [10] Menard J. *et al* 2012 Overview of the physics and engineering design of NSTX upgrade *Nucl. Fusion* **52** 083015
- [11] Kaye S., Gerhardt S., Guttenfelder W., Maingi R., Bell R., Diallo A., LeBlanc B. and Podesta M. 2013 The

- dependence of H-mode energy confinement and transport on collisionality in NSTX *Nucl. Fusion* **53** 063005
- [12] Canik J.M., Guttenfelder W., Maingi R., Osborne T.H., Kubota S., Ren Y., Bell R.E., Kugel H.W., LeBlanc B.P. and Souhkanovskii V.A. 2013 Edge microstability of NSTX plasmas without and with lithium-coated plasma-facing components *Nucl. Fusion* 53 113016
- [13] Candy J., Waltz R.E. and Dorland W. 2004 The local limit of global gyrokinetic simulations *Phys. Plasmas* 11 L25–L28
- [14] Giacomin M., Kennedy D., Casson F.J., Ajay C.J., Dickinson D., Patel B.S. and Roach C.M. 2024 On electromagnetic turbulence and transport in STEP *Plasma Phys. Control. Fusion* 66 055010
- [15] Sharma A.Y. et al 2022 Global gyrokinetic study of shaping effects on electromagnetic modes at NSTX aspect ratio with ad hoc parallel magnetic perturbation effects *Phys. Plasmas* 29 112503
- [16] Dominski J., Guttenfelder W., Hatch D., Gørler T., Jenko F., Munaretto S. and Kaye S. 2024 Global micro-tearing modes in the wide pedestal of an NSTX plasma *Phys. Plasmas* 31 044501
- [17] Ren Y. et al 2020 Exploring the regime of validity of global gyrokinetic simulations with spherical tokamak plasmas Nucl. Fusion 60 026005
- [18] Tang W.M., Connor J.W. and Hastie R.J. 1980 Kinetic-ballooning-mode theory in general geometry *Nucl. Fusion* 20 1439
- [19] Lin Z., Hahm T.S., Lee W.W., Tang W.M. and White R.B. 1998 Turbulent transport reduction by zonal flows: massively parallel simulations *Science* 281 1835
- [20] Xiao Y., Holod I., Wang Z.X., Lin Z. and Zhang T.G. 2015 Gyrokinetic particle simulation of microturbulence for general magnetic geometry and experimental profiles *Phys. Plasmas* 22 022516
- [21] Wang Z., Lin Z., Holod I., Heidbrink W.W., Tobias B., Van Zeeland M. and Austin M.E. 2013 Radial localization of toroidicity-induced Alfvén eigenmodes *Phys. Rev. Lett.* 111 145003
- [22] Bao J., Lin Z., Kuley A. and Lu Z.X. 2014 Particle simulation of lower hybrid wave propagation in fusion plasmas *Plasma Phys. Control. Fusion* 56 095020
- [23] Zhang W., Lin Z. and Chen L. 2008 Transport of energetic particles by microturbulence in magnetized plasmas *Phys. Rev. Lett.* 101 095001
- [24] Singh T., Sharma D., Macwan T., Sharma S., Ghosh J., Sen A., Lin Z. and Kuley A. 2023 Gyrokinetic simulation of electrostatic microturbulence in ADITYA-U tokamak *Nucl.* Fusion 63 056008
- [25] Singh T. et al 2024 Gyrokinetic simulations of electrostatic microturbulence in ADITYA-U tokamak with argon impurity Nucl. Fusion 64 086038
- [26] Wang H.Y., Holod I., Lin Z., Bao J., Fu J.Y., Liu P.F., Nicolau J.H., Spong D. and Xiao Y. 2020 Global gyrokinetic particle simulations of microturbulence in W7-X and LHD stellarators *Phys. Plasmas* 27 082305
- [27] Singh T., Nicolau J.H., Lin Z., Sharma S., Sen A. and Kuley A. 2022 Global gyrokinetic simulations of electrostatic microturbulent transport using kinetic electrons in LHD stellarator *Nucl. Fusion* 62 126006
- [28] Dong G., Bao J., Bhattacharjee A. and Lin Z. 2019 Nonlinear saturation of kinetic ballooning modes by zonal fields in toroidal plasmas *Phys. Plasmas* 26 010701
- [29] Liao X., Lin Z., Holod I., Xiao Y., Li B. and Snyder P.B. 2016 Microturbulence in DIII-D tokamak pedestal. III. Effects of collisions, *Phys. Plasmas* 23 122507
- [30] McClenaghan J. et al 2025 Role of parallel magnetic field effects in predicting turbulent transport in NSTX Plasma Phys. Control. Fusion 67 055013

[31] Lee W.W. 1987 Gyrokinetic particle simulation model *J. Comput. Phys.* **72** 243

- [32] Dong G., Bao J., Bhattacharjee A., Brizard A., Lin Z. and Porazik P. 2017 Gyrokinetic particle simulations of the effects of compressional magnetic perturbations on drift-Alfvénic instabilities in tokamaks *Phys. Plasmas* 24 081205
- [33] Brizard A.J. and Hahm T.S. 2007 Foundations of nonlinear gyrokinetic theory *Rev. Mod. Phys.* 79 421
- [34] Parker S.E. and Lee W.W. 1993 A fully nonlinear characteristic method for gyrokinetic simulation *Phys. Fluids B* 5 77–86
- [35] Deng W., Lin Z. and Holod I. 2012 Gyrokinetic simulation model for kinetic magnetohydrodynamic processes in magnetized plasmas *Nucl. Fusion* 52 023005
- [36] Holod I., Zhang W.L., Xiao Y. and Lin Z. 2009 Electromagnetic formulation of global gyrokinetic particle simulation in toroidal geometry *Phys. Plasmas* 16 122307
- [37] Chen Y.C., Qin Y.Q., Sun G.Y., Dong G., Xiao Y. and Lin Z. 2023 Effects of radial electric field on kinetic ballooning mode in toroidal plasma *Phys. Plasmas* 30 022302
- [38] Lin Z., Nishimura Y., Xiao Y., Holod I., Zhang W.L. and Chen L. 2007 Global gyrokinetic particle simulations with kinetic electrons *Plasma Phys. Control. Fusion* 49 12B
- [39] Hawryluk R.J. et al 1980 An Empirical Approach to Tokamak Transport, Physics of Plasmas Close to Thermonuclear Conditions vol 1, ed B. Coppi (CEC)) pp 19–46
- [40] Gerhardt S.P., Andre R. and Menard J.E. 2012 Exploration of the equilibrium operating space for NSTX-Upgrade *Nucl. Fusion* 52 083020
- [41] Xie H.S., Xiao Y., Holod I., Lin Z. and Belli E.A. 2016 Sensitivity of kinetic ballooning mode instability to tokamak equilibrium implementations J. Plasma Phys. 82 905820503
- [42] Lao L.L., Ferron J.R., Groebner R.J., Howl W., John H., Strait E.J. and Taylor T.S. 1990 Equilibrium analysis of current profiles in tokamaks *Nucl. Fusion* 30 1035
- [43] Wei X. *et al* Formulations and verification of gyrokinetic simulation of kinetic-MHD processes in toroidal plasmas (arXiv:2109.08873)
- [44] Rafiq T., Wilson C., Clauser C., Schuster E., Weiland J., Anderson J., Kaye S.M., Pankin A., LeBlanc B.P. and Bell R.E. 2024 Predictive modeling of NSTX discharges

- with the updated multi-mode anomalous transport module *Nucl. Fusion* **64** 076024
- [45] Gates D.A. et al 2006 Effect of plasma shaping on performance in the National Spherical Torus Experiment Phys. Plasmas 13 056122
- [46] Belli E.A., Hammett G.W. and Dorland W. 2008 Effects of plasma shaping on nonlinear gyrokinetic turbulence *Phys. Plasmas* 15 092303
- [47] Kinsey J.E., Waltz R.E. and Candy J. 2007 The effect of plasma shaping on turbulent transport and $\vec{E} \times \vec{B}$ shear quenching in nonlinear gyrokinetic simulations *Phys. Plasmas* **14** 102306
- [48] Ida K. 2023 Isotope effect of transport and key physics in the isotope mixture plasmas *Rev. Mod. Plasma Phys.* **7** 23
- [49] Yang Y., Ye L., Chen Y., Xiang N. and Sun Y. 2023 Gyrokinetic particle-in-cell simulation of the effect of compressional magnetic perturbations on the microscopic instabilities in tokamak *Comput. Phys. Commun.* 292 108892
- [50] Beeke O., Barnes M., Romanelli M., Nakata M. and Yoshida M. 2021 Impact of shaping on microstability in high-performance tokamak plasmas *Nucl. Fusion* 61 066020
- [51] Xiao Y. and Lin Z. 2009 Turbulent transport of trapped-electron modes in collisionless plasmas *Phys. Rev.* Lett. 103 085004
- [52] Hahm T.S., Diamond P.H., Lin Z., Itoh K. and Itoh S.-I. 2004 Turbulence spreading into the linearly stable zone and transport scaling *Plasma Phys. Control. Fusion* 46 A323
- [53] Waltz R.E. and Candy J. 2005 Heuristic theory of nonlocally broken gyro-Bohm scaling *Phys. Plasmas* 12 072303
- [54] Gørler T. et al 2011 Flux- and gradient-driven global gyrokinetic simulation of tokamak turbulence Phys. Plasmas 18 056103
- [55] Wan W., Parker S.E., Chen Y., Groebner R.J., Yan Z., Pankin A.Y. and Kruger S.E. 2013 Global gyrokinetic simulations of the H-mode tokamak edge pedestal *Phys. Plasmas* 20 055902
- [56] Singh T., Nicolau J.H., Nespoli F., Motojima G., Lin Z., Sen A., Sharma S. and Kuley A. 2024 Global gyrokinetic simulations of electrostatic microturbulent transport in LHD stellarator with boron impurity *Nucl. Fusion* 64 016007